Research paper

Forest 2200 nm/660 nm reflectance seasonality for improved satellite-image atmospheric correction

Mait Lang[1,2]*, Lea Hallik[1] and Allan Sims[2]

Lang, M., Hallik, L., Sims, A. 2025. Forest 2200 nm/660 nm reflectance seasonality for improved satellite-image atmospheric correction. – Forestry Studies | Metsanduslikud Uurimused 82, 1–19, ISSN 1736-8723. Journal homepage: http://mi.emu.ee/forestry.studies

Abstract. A widely used algorithm, Sen2Cor, for the atmospheric correction of Sentinel-2 MSI images assumes a constant ratio of red (0.6 µm) and near-infrared (2.2 µm) spectral reflectance, taking $\rho_{2.2}/\rho_{0.6}$ = 2. In fact, however, this ratio exhibits substantial dependence on vegetation phenology. The discrepancy produces errors in predicted surface reflectance. We analyse the reflectance of 92,230 forest stands, using full time series of Landsat-8/9 OLI and Sentinel-2 MSI images taken over Estonia. We find the $\rho_{2.2}/\rho_{0.6}$ value for evergreen needleleaf forests to be rather stable over time, with a mean value around 2.25. In broadleaf deciduous forests, on the other hand, we find $\rho_{2.2}/\rho_{0.6}$ to increase rapidly in the spring, to remain on average close to 3 or greater, and then to decrease in the autumn. We offer parametric and tabulated models of $\rho_{2.2}/\rho_{0.6}$ for eventual integration with Sen2Cor.

Key words: phenology, Landsat, Sentinel, dense vegetation, Sen2Cor.

Authors' addresses: [1]Tartu Observatory, University of Tartu, 61602 Tõravere, Estonia; [2]Institute of Forestry and Engineering, Estonian University of Life Sciences, Kreutzwaldi 5, 51006 Tartu, Estonia; *e-mail: lang@to.ee

Introduction

Optical (300 to 2500 nm) electromagnetic-spectrum observations of the Earth's surface from spacecraft are influenced by the absorption of atmospheric gases, by Rayleigh scattering from gas molecules, and by scattering and absorption processes involving the various small particles that constitute aerosols (Turner & Spencer, 1972). To correct for the atmospheric influence, it is necessary to know at least the amounts of atmospheric ozone and water vapour and the optical depth of aerosols (the visibility). A simple method for atmospheric correction assumes that for a dark target exhibiting some known very small reflectance, most of the recorded signal is related to the atmosphere (Chavez, 1988). Clear water absorbs solar radiation intensely and therefore can serve as a dark target. Finding sufficiently well characterizable dark targets for land observations, on the other hand, is problematic.

Kaufman *et al.* (1997) proposed taking dense vegetation as a dark target. Upon analysing Landsat-5 Thematic Mapper images and Airborne Visible/Infrared Imaging Spectrometer (AVIRIS) measurements taken on clear days, they found that reflectance in the red spectral region (0.6 µm) can be predicted by a simple and strong correlation from near-infrared (2.2 µm) reflectance. The estimated ratio $\rho_{2.2}/\rho_{0.6}$ = 2 was proposed for the Terra MODIS operational algorithm (Kaufman *et al.*, 1997) and was later suggested for Landsat data (Liang *et al.*, 1997), with implementation improvements added by Ouaidrari & Vermote (1999).

Subsequent studies by Remer *et al.* (2001) and Gatebe *et al.* (2001) found that in general the assumption $\rho_{2.2}/\rho_{0.6}$ = 2 holds reasonably well. However, they also reported dependence of $\rho_{2.2}/\rho_{0.6}$ on measurement and illumination geometry, on vegetation type, and on growth season. Remer *et al.* (2001) found that the forest $\rho_{2.2}/\rho_{0.6}$ value can double when tree growth reaches its summer maximum. Kaufman *et al.* (2002) carried out a series of model simulation experiments and explained in a comprehensive way the principal factors influencing $\rho_{2.2}/\rho_{0.6}$, as identified in empirical studies: canopy cover, soil brightness, leaf area index, and measurement geometry. They concluded that the assumption $\rho_{2.2}/\rho_{0.6}$ = 2 is robust enough to

DOI: 10.2478/fsmu-2025-0001

© 2025 by the authors. Licensee Estonian University of Life Sciences, Tartu, Estonia. This article is an open access article distributed under the terms and conditions of the Creative Commons Attribution (CC BY) license (http://creativecommons.org/licenses/by/4.0/).

be used in operational algorithms for satellite-data atmospheric correction.

Levy *et al.* (2007) implicitly added into the MODIS algorithm modifications of the $\rho_{2.2}/\rho_{0.6} = 2$ assumption based on the scattering angle and canopy vegetation index. The same modifications were adopted for the Landsat-8/9 OLI algorithm LaSRC by Vermote *et al.* (2016). Remer *et al.* (2020) conclude in their review, based on collected datasets, that although the assumption $\rho_{2.2}/\rho_{0.6} = 2$ represents a global average sufficiently well, there is substantial scatter around the assumed constant relationship. This scatter may be more pronounced in regions where vegetation exhibits strong seasonal phenology. In many places, the (automatically) selected dark dense vegetation is most likely forest. Boreal and hemiboreal forests cover large territories and exhibit significant phenology in their reflectances (Suviste *et al.*, 2007; Nilson *et al.*, 2008, 2012; Rautiainen *et al.*, 2018).

The atmospheric correction algorithm for Sentinel-2 MSI data for its part again assumes $\rho_{2.2}/\rho_{0.6} = 2$.

Landsat and Sentinel data are employed in national forest inventories for change detection and the estimation of forest structure variables. Since atmospheric correction results depend on predicted reflectance for the dark reference, deviations from the assumed constant $\rho_{2.2}/\rho_{0.6}$ value introduce uncertainties into forest spectral reflectance predictions. In response to this difficulty, our study focuses on the time series of Sentinel-2 MSI and Landsat-8/9 OLI images. We analyse the seasonal dependence of $\rho_{2.2}/\rho_{0.6}$, examining 92,230 forest stands in Estonia. We propose models for predicting the (nonconstant) ratio to be used in improved atmospheric correction algorithms.

Material and Methods

Study site

The target area, in south and south-east Estonia, lies between longitudes 24.5° E and 28.3° E and between latitudes 57.5° N and 59.6° N. The ground-surface topography is flat, with ground elevation rising only to 318 m above mean sea level (Arold, 2005). The landscape in this part of Estonia is characterised by hills with a local relative height exceeding tens of metres (Arold, 2005).

The forests in the test area are predominantly composed of evergreen coniferous Norway spruce (*Picea abies* (L.) H. Karst.) and Scots pine (*Pinus sylvestris* L.), and of broadleaf deciduous European aspen (*Populus tremula* L.), silver birch (*Betula pendula* Roth), downy birch (*Betula pubescens* Ehrh.), grey alder (*Alnus incana* (L.) Moench), and black alder (*Alnus glutinosa* (L.) Gaertn.) (Valgepea *et al.*, 2023). Within the test area, diverse forest site types and plant species compositions are developed over various mineral soils (Leptosols, Cambisols, Luvisols, Albeluvisols, and Podzols), and additionally over Histosols (Kõlli *et al.*, 2004). According to Valgepea *et al.* (2023), the Estonian National Forest Inventory estimates a forest cover of 53.5% for Estonia as a whole.

Forest stand height in the test area generally remains below 35 m (Tappo, 1982). Multi-layer forests are common, with Norway spruce and other shade-tolerant species growing below the upper canopy. The average stand size is 1.24 ha. Within the test area larger stands occur more frequently in state forests (Valgepea *et al.*, 2023). After stand-replacing disturbances, tree regeneration develops dense canopy covers, usually during the first 10 years. In the case of managed forests within the test area, canopy cover may be modified with thinnings and maintenance fellings.

The test area exhibits a diverse range of landscapes, shaped by legal restrictions on clear-cut sizes – ranging from 2 to 7 ha depending on forest type (Forest Act, 2023) – and by a long-standing tradition of retention forest management (Gustafsson *et al.*, 2012) that promotes rapid regeneration on forest land. Within Estonia as a whole, forest management is limited or entirely prohibited over a remarkable 30.3% of forest land (Raudsaar *et al.*, 2023).

Phenology of dominant tree species

The four seasons characteristic of the study area drive its vegetation growth (Jaagus & Ahas, 2000). While observable signs of springtime greening occur in the forest understorey vegetation by mid-April, the active development of new leaves on trees starts by mid-May. The summertime season peak is attained by the end of June, after which growth continues until some point in the first 10 days of September, when the first occurrences of leaf yellowing become evident. By the end of October, the deciduous trees have shed most of their leaves. The timing of the phenophases is spatially variable in Estonia, over a range of about 10 days (Jaagus & Ahas, 2000). The phenophases of forest trees are influenced by tree genotype, and even more by year-to-year differences in air temperature (Possen *et al.*, 2014), which in this region correlate with the North Atlantic oscillation (NAO) and Arctic oscillation (AO) indices (Aasa *et al.*, 2004).

Scots pine in Estonia starts to develop current-year shoots around DOY 132 (EE, 2025). Scots pine has an intensive needle-shedding period in the middle of September, after which only needles from the last two years remain over the winter (Kollist, 1967).

Norway spruce exhibits two well-known phenological forms in Estonia (Sellin *et al.*, 2024), with the average DOYs for budburst on branches cited as 142 and 153 for the early- and late-flushing trees, respectively, and budburst of top shoot few days later. Some phenological observations, however, indicate a somewhat earlier time, with DOY = 138 (EE, 2025). The average DOYs of top-shoot growth cessation are 185 and 190 in the early- and the late-flushing spruces, respectively, whereas the respective DOYs for growth cessation of branches are 175 and 185. In contrast with Scots pine, Norway spruce needles undergo no massive, visually detectable, autumnal yellowing.

European aspen likewise exhibits early- and late-flushing phenological forms in Estonia. Foliation starts around DOY 132, can in some years be delayed by a week or two, and lasts for about 14 days (Tamm, 2000). Autumn colouring appears in the first leaves in September, becoming fully evident by DOY 266 (EE, 2025). Dormancy is reached on DOY 289 (EE, 2025).

Two birch species, silver birch and downy birch, are included in our forest inventory data without being distinguished. Downy birch dominates on poor soils, whereas silver birch occupies most of the fertile soils. On average, birch leaf formation starts on DOY 126 (Jaagus & Ahas, 2000), or according to the phenology calendar (EE, 2025) a few days later, on DOY 130. Our own observations indicate that leaf unfolding is delayed by about a week on wet and poor soils, since these warm more slowly, hindering the start of active growth. Autumn colouring starts in the first leaves by the end of August, becoming fully evident by DOY 262. Dormancy is reached on DOY 295 (EE, 2025).

Grey alder is described in the phenology calendar (EE, 2025) as follows: bud swelling starts on DOY 109, autumn leaf colouring is fully observable on DOY 271, and dormancy is reached on DOY 262. Our own observations indicate that autumn colouring of grey alder foliage yields brownish tones, in contrast with the yellow of silver birch and the yellow-red mixture of European aspen.

Forest register and inventory data

The Estonian Environment Agency (Keskkonnaagentuur) maintains the Estonian forest register (Eesti metsaregister). The database contains forest management inventory data in tabular form, accompanied by 1:10,000 stand border maps. We used state forest records taken from the database in the version of 08 February 2023 to select stands that are sufficiently large in relation to 30 m pixels in satellite images. Our database query conditions were as follows: stand age greater than 15 years; stand area between 1 and 10 ha; and relative stocking density (this correlates strongly with canopy cover) greater than 80%, including both the upper and second tree layer.

We made the selection from the list of stands dominated by Norway spruce, Scots pine, European aspen, birch species, and grey alder. Black alder stands were not included, because preliminary experiments with the satellite-image atmospheric correction algorithm revealed black alder stands to be not selected as dense dark vegetation.

Tree species groups

For the analysis of seasonal changes in $\rho_{2.2}/\rho_{0.6}$, the selected forest stands were assigned tree species group labels, the various groups being defined by soil fertility and dominant tree species (Table 1). The final selection of stands was made only after queries from raster layers in the satellite images, to ensure that only those stands were included that had more than 70% of their area covered by pixels with centroids inside the stand polygons. This exclusion rule eliminated stands of irregular shape and minimised the influence of mixed pixels located at stand borders. Table 2 gives sample sizes and mean values of forest inventory variables. Norway spruce contributes notably to species composition in the deciduous broadleaved group (9%) and in the pine stands growing on fertile soils (7%), because Norway spruce is shade-tolerant, frequently growing as a second layer below the light-demanding deciduous broadleaved species, and also frequently growing on fertile soils below stands of Scots pine. The mean normalised difference vegetation index (NDVI) in our selected forest areas is 0.79, with standard deviation of 0.09 (Table A3.1), when calculated for the active growth season ($140 < \text{day} < 260$).

Satellite images

Landsat-8/9 OLI (Zanter, 2016; Sayler & Glynn, 2022) collection 002 images that were processed to level L1 (at-sensor radiance) and L2 (surface reflectance) were downloaded from the USGS GLOVIS data server. The Sentinel-2A/B MSI images of the latest available baseline processing with versions starting from 04.00 (https://sentiwiki.copernicus.eu/web/s2-processing) were downloaded from the

Table 1. Construction rules for tree-species groups. The fertility classes correspond to Orlov's bonity categories, where 0 indicates the greatest and 6 the lowest fertility. The bonity class 3 is excluded from soil fertility-dependent subsets. Forest inventory data do not distinguish between silver birch and downy birch. However, it is known that downy birch dominates on poor soils.

Tabel 1. Reeglid puistute rühmitamiseks. Kolmanda boniteediklassiga puistud jäeti välja mullaviljakuse mõju testimise gruppidest.

Group *Grupp*	Species *Liigid*	Share (%) *Osakaal (%)*	Fertility classes *Boniteediklassid*
All stands	All	All	all
Evergreen needleleaved	Norway spruce, Scots pine	≥ 85	all
Deciduous broadleaved	Norway spruce excluded, Scots pine excluded	≥ 85	all
Pine	Scots pine	≥ 80	all
Pine (fertile soil)	Scots pine	≥ 80	0, 1, 2
Pine (poor soil)	Scots pine	≥ 80	4, 5, 6
Birch spp.	Silver birch, downy birch	≥ 80	all
Birch (fertile soil)	Silver birch	≥ 80	0, 1, 2
Birch (poor soil)	(Silver birch), downy birch	≥ 80	4, 5, 6
Spruce	Norway spruce	≥ 80	all
Aspen	European aspen	≥ 75	all
Alder	Grey alder	≥ 75	all

Table 2. Detailed descriptions of the tree species groups introduced in Table 1. KU signifies Norway spruce, MA Scots pine, HB European aspen, KS both silver birch and downy birch (these two species are not distinguished in the forest inventory of the Estonian Environment Agency), LV grey alder, and KX species compositions not matching any of the other codes. Stands in the evergreen needleleaf group Everg. N. consist predominantly of Norway spruce and Scots pine, while stands in the group Dec. Br. are dominated by deciduous broadleaved species. In the Bon (bonity) column, code A signifies all fertility classes, P poor soils, and F fertile soils. For each tree species group, an entry in the N column gives the number of stands in that group, S its aggregate area, A the mean value of its various stand ages, H_{100} the mean value of the 100-year heights predicted for its various stands (this is a measure of site productivity), T its relative density, and G its basal area.

Tabel 2. Analüüsiks moodustatud vaatluste grupid. Puuliikide lühendid on metsakorralduse juhendi järgi, KX tähistab muid liike. Igihaljad okaspuud on grupis „Everg. N." ja heitlehiste lehtpuude grupp on „Dec. Br.". Gruppide moodustamise reeglid on tabelis (1). Kirjeldavad tunnused on: puistute arv (N), kogupindala (S), keskmine vanus (A), keskmine kõrgusindeks H_{100}, keskmine täius (T) ja keskmine rinnaspindala (G).

Group *Grupp*		Stands *Eraldised*		Stand structure *Puistute struktuur*				Tree species composition (%) *Keskmine liigiline koosseis (%)*					
Species	Bon	N	S (ha)	A	H_{100} (m)	T (%)	G ($m^2\,ha^{-1}$)	HB	KS	KU	LV	MA	KX
All	A	92,230	231,687	77	26.6	94	28.4	6	29	26	3	33	3
Everg. N.	A	34,073	83,321	92	25.4	92	30.4	0	4	28	0	68	0
Dec. Br.	A	22,659	60,990	61	27.1	95	25.4	13	60	9	8	1	9
MA	A	1,5898	39,765	94	23.4	90	29.7	0	3	5	0	92	0
MA	F	8,675	20,553	85	27.2	91	31.1	0	3	7	0	90	0
MA	P	3,388	9,575	107	15.8	89	26.6	0	3	2	0	95	0
KU	A	5,092	11,627	51	31.3	93	27.7	1	6	90	1	1	1
KS	A	6,471	17,024	56	24.8	93	21.7	1	90	4	1	2	2
KS	F	4,013	10,130	50	27.3	93	22.6	1	90	5	1	1	2
KS	P	6,66	1,978	69	17.6	94	18.5	0	91	2	0	4	3
HB	A	441	951	65	31.7	95	31.7	83	8	6	1	0	2
LV	A	960	2,222	45	27.0	96	25.8	2	5	3	88	0	2

Estonian Land Board (Maa- ja Ruumiamet) data hub. The Sentinel-2 MSI data corresponded to at-sensor reflectance at the processing level L1C.

An inspection revealed that the USGS Landsat-8/9 OLI surface reflectance dataset was influenced by a production error that expressed itself as a noise pattern deriving from the aerosol estimation quality map in the red spectral region and even in the near-infrared. For this reason, USGS Landsat-8/9 OLI surface reflectance data (L2) were not used for forest stand-level analysis, but only for determining the $\rho_{2.2}/\rho_{0.6}$ mean value across each image. The image-wide dark dense-vegetation mean reflectance values were used only to estimate the initial parameters for our $\rho_{2.2}/\rho_{0.6}$ phenology model: USGS applies a phenology-dependent algorithm (Vermote *et al.*, 2016) for atmospheric correction, in contrast with the Sen2Cor3 algorithm (Pignatale *et al.*, 2025) employed in this study to process both Landsat-8/9 OLI L1 and Sentinel-2 MSI L1C data.

In the case of Landsat-8/9 OLI, this study used images from WRS-2 system paths and rows 185–019, 185–020, 186–019, 186–020, 187–018, 187–019, and 187–020. In the case of Sentinel-2 MSI, this study used image granules from the locations of MGRS-2 system tiles T35VME and T35VNE. Our decision in both cases was driven by the availability of stationary AERONET (https://aeronet.gsfc.nasa.gov) and SkySpec (Kuusk & Kuusk, 2018) radiometers that provided data for the preliminary assessment of atmospheric correction of satellite images, in work parallelling Doxani *et al.* (2023). However, when our study progressed beyond this preliminary assessment, we did not find it necessary to analyse the statistical correlations between the radiometer data and aerosol optical depth estimates from the satellite images.

In selecting a satellite image for the study, we required that the usable area, net of obscuration by clouds, be greater than about 25% of the image area. The sampling period started each year in March, with the consequent inclusion of images that may on a local scale have exhibited some remaining small traces of snow in shaded pixels at forest edges. Each year, the sampling period ended on the last day of October. In the process of image selection, the entire time series, starting in 2013 and ending in 2024, was checked visually. The number of days when the overpass of at least one satellite yielded usable image data was 268. This total, however, includes days when both satellites made overpasses of the study area: in the entire sequence of selected images, there were 122 Landsat-8/9 overpasses and 146 Sentinel-2 overpasses.

All satellite images were used in their original map projection. Forest stand boundaries were reprojected for each individual image to avoid errors from the resampling of raster data. High-quality cloud and cloud-shadow masks were constructed for the Sentinel-2 MSI images with KappaMask (Domnich *et al.*, 2021). Our assessment supplied additional confirmation that this algorithm has substantially greater precision than other algorithms. In the case of Landsat-8/9 OLI, the cloud masks bundled with the spectral data were later additionally used in the Sen2Cor3 runs, as the masks were superior to the native Sen2Cor3 algorithm in detecting faint clouds and faint cloud shadows.

The atmospheric correction program Sen2Cor3

The Sen2Cor3 (Pignatale *et al.*, 2025) tool is a version of the official atmospheric correction program Sen2Cor distributed by the European Space Agency and maintained by its partners. Sen2Cor is deployed worldwide in data hubs and by Sentinel-2 MSI data users for predicting ground surface reflectance from top-of-atmosphere (TOA) reflectance measurements (ESA, 2021). Sen2Cor3 is developed within the Sen2Like project (Saunier *et al.*, 2022) and includes an option to process also Landsat-8/9 TOA data and calculate surface reflectance.

We downloaded the latest Sen2Cor3 version 3.01.00, available in August 2024, according to the instructions given in GitHub (https://github.com/senbox-org/sen2like/blob/master/sen2cor3/README.md), installing it on a Linux workstation. This software, written in Python, is provided as open-source code, apart from the module for calculating topographic shadows.

Initial test runs indicated the possibility of improving the preprocessing phase, run by Sen2Cor3 as a preliminary to its atmospheric correction. In this preprocessing, Sen2Cor3, proceeding on the basis both of reflectance $\rho_{2.2,ref}$ in the near-infrared (2.2 μm) band and of other filters, selects pixels that are assumed to represent dense dark vegetation (DDV). First, we replaced the three-step adjustment of threshold imposed on a preliminary estimate of $\rho_{2.2,ref}$ by Sen2Cor3 in its DDV-pixel selection phase with a small-step incremental search for the threshold value. Our search used the same three configurable decision thresholds as are provided with the program configuration files described in the Sen2Cor3 manual. In place of the commonly used value $\rho_{2.2,ref} = 0.05$, however, we set the first threshold to the lower value of 0.035.

Second, we added a binary morphology-based filter to remove small putative DDV-pixel groups that were found upon visual inspection of the DDV maps to consist mostly of noise. We constructed our filter by combining SciPy library procedures that do binary erosion, setting the parametric window structure size to 2 × 2 pixels, and a binary propagation operation. We found that our filter effectively removed salt-and-pepper noise from the DDV map without generating the geometric distortions typical in the case of moving window-based median filters.

This pair of enhancements yielded a large improvement in the consistent detection of DDV pixels, as the target optimum of 2% out of the total number of pixels of interest: the DDV set was now more efficiently targeted, without the occasional large incremental steps in the DDV-pixel set size generated by the original algorithm.

However, test runs under our two enhancements now revealed that DDV pixels were frequently selected from areas of cloud shadow not identified by the Sen2Cor algorithm. This problem was in turn addressed with a third modification, by importing data for clouds and cloud shadows from KappaMask, as applied on the one hand to the Sentinel images, on the other hand to the Landsat L1 pixel-quality metadata layer bundled with images in the Landsat product. Our selection of DDV pixels was allowed only for terrain lying outside the buffers of 600 m for Sentinel-2 MSI and 1500 m for Landsat-8/9OLI.

Our three enhancements jointly added about 10 seconds of processing time per image tile to the total of 15 to 25 minutes originally required.

As a filter throughout its processing, Sen3Cor uses surface-elevation maps (for the calculation of vertical visibility in the atmosphere) and water-body maps. In place of the coarse-scale datasets included within the Sen2Cor3 installation package, we used the ground-surface digital elevation model, at fine-scale (25 m) spatial resolution, with a 1:10,000 water body map (showing lakes and rivers) provided by the Estonian Land Board. To avoid the selection of mixed-landcover pixels as dark dense vegetation, the water body map was rasterised, and a buffer was added around water bodies.

The atmospheric correction procedure requires data for ozone and water vapour content. In the case of Sentinel-2 MSI, the ozone data is bundled with the image, and a water-vapour map is predicted with an internal algorithm of Sen2cor3. In the case of Landsat OLI, the Copernicus Atmosphere Monitoring System (CAMS) data (https://atmosphere.copernicus.eu/) could be used. Although this functionality was not yet fully included in the Sen2Cor3 version 3.01.00, the Telespazio team kindly provided us with code from the development version of the next Sen2Cor3 release. This Sen2Cor3 upgrade allowed us to read ozone and water vapour data from daily CAMS data, instead of setting some values manually for each individual image.

Finally, we added functionality for setting the target region of interest (ROI) for DDV-pixel selection, through a vector polygon file. We constructed this ROI by adding a 30 km positive buffer around the Estonian state border, thereby excluding from the images localities contaminated by haze outside our study area. Because hazy atmospheres exhibit trends in their optical properties, the imaging of such contaminated localities would bias otherwise usable pixels. Specifically, bias would be introduced by the fact that Sen2Cor uses mean aerosol optical depth per granule instead of the map (for reasons yet unknown to us: the algorithm duly constructs the map in its internal operations, while leaving it unused).

The processing of the entire image time series took on the order of 12 or 13 hours on a Linux workstation running the OpenSUSE 15.5 operating system, with 16 CPU cores, 128 GB of RAM, and a NVIDIA GeForce 630 graphics card fitted with its own 2 GB of RAM. System tools were used to run from 12 to 14 Sen2Cor3 instances in parallel, with each instance processing a single image granule.

The image processing and band ratio phenology analysis

With the enhanced Sen2Cor3 all images were first processed under standard settings, except that the initial threshold for $\rho_{2.2,ref}$ was specified as 0.035 in place of the standard value 0.05. The $\rho_{2.2}/\rho_{0.6}$ ratio was kept at the constant value 2, corresponding to the value 0.5 given in the program input-configuration file. This first run produced DDV-pixel maps.

The DDV maps were then used to sample pixels from the USGS version of the Landsat-8/9 OLI surface-reflectance data. This sampling step was appropriate because the LaSRC algorithm (Vermote *et al.*, 2016) uses coarse-resolution reflectance data time series collected from a selection of MODIS and MISR images (with pixel size of about 5 km × 2.5 km at our study area) to determine band ratios for particular regions and seasons: consequently, the USGS Landsat-8/9 OLI level L2 dataset, for which LaSRC considers the seasonality of

ground-surface spectral reflectance, should in theory outperform Sen2Cor in capturing the seasonal changes in plant canopy reflectance. The mean $\rho_{2.2}/\rho_{0.6}$ ratio was calculated for each Landsat-8/9 OLI granule, and to this data the following modified double logistic model (Eklundh & Jönsson, 2012) was fitted:

$$\rho_{2.2}/\rho_{0.6} = a + \frac{1}{b + \exp\left(\frac{k_{pk} - t}{k_k}\right)} - \frac{c}{d + \exp\left(\frac{k_{ps} - t}{k_s}\right)} + \varepsilon, \quad (1)$$

where ε is the model residual error (RSE); t is the day number in the year; a, b, c, and d are free parameters; k_{pk} is the springtime inflection point; k_k is the springtime growth rate; k_{ps} is the autumn inflection point; and k_s is the autumn growth rate. The values of k_{pk}, k_k, k_{ps}, and k_s were first found by expert guess, after which a, b, c, and d were estimated with the nls procedure in R (R Core Team, 2022; Baty *et al.*, 2015), version 4.2.2. The obtained model estimates, with 100 degrees of freedom and the residual standard error 0.087, were as follows: a = 1.81, b = 6.51, c = 0.379, d = 0.785, k_{pk} = 140, k_k = 5, k_{ps} = 260, and k_s = 25.

Next, the model was fitted to the surface-reflectance data that had been obtained from the first run of Sen2Cor3 (described above), with its assumption of constant $\rho_{2.2}/\rho_{0.6}$ = 2. The empirical dataset for this fitting step consisted of DDV pixels aggregated (binned) for each image by unique $\rho_{2.2}$ values, to decrease the data size. The group mean $\rho_{0.6}$ was calculated for each bin, with the number of pixels in the bin used as a weight in model parameter estimation. The parameters k_{pk}, k_k, k_{ps}, and k_s were fixed to the values found for the USGS Landsat L2 dataset. The free parameters a, b, c, and d were again estimated with the nls procedure in R. After this revision, the model estimates, with 168,484 degrees of freedom and the residual standard error 9.4, were as follows: a = 2.08, b = 6.85, c = 0.40, d = 1.1, k_{pk} = 140, k_k = 5, k_{ps}, = 260, and k_s = 25. The notable large residual error arose because here the DDV pixel groups were the observations.

With the model (1) predictions checked against data scatter plots, the model was found suitable. The model was then used with the adopted parameter estimates to make predictions of $\rho_{2.2}/\rho_{0.6}$ for all the images in our dataset. Atmospheric correction of top-of-atmosphere radiance data was done again with Sen2Cor3, but now dropping the assumption of the constant channel ratio and using instead the DOY-dependent $\rho_{2.2}/\rho_{0.6}$.

Finally, the atmospherically corrected images served to sample forest spectral reflectance, using forest stands as delineated in the forest inventory map. The empirical dataset for studying $\rho_{2.2}/\rho_{0.6}$ seasonal variability was constructed by selecting the stands that had (as previously described) more than 70% of their area covered by reflectance data pixels with centroids inside the stand polygons. An additional filter was now imposed, excluding those areas in each image that were less than 1 km away from clouds and cloud shadows.

At this stage the model (1) was fitted for each tree species group (Table 1, Table 2), so that single observation corresponded to the $\rho_{2.2}/\rho_{0.6}$ of an individual forest stand calculated from a particular image granule. The search ranges for the model parameters k_{pk}, k_k, k_{ps}, and k_s were allowed to vary reasonably widely around the previous estimates. The search ranges for a, b, and d had to be limited for some species groups. The parameter c was throughout this fitting fixed to the constant c = 1. The coefficient of determination R^2 was calculated as

$$R^2 = \frac{\sum(y_i - \hat{y}_i)^2}{\sum(y_i - \bar{y})^2}, \quad (2)$$

where y_i is the $\rho_{2.2}/\rho_{0.6}$ value for a single stand on an image granule, $\hat{y}_i$ is the predicted value, and $\bar{y}$ is the species-group sample mean. The model (1) was incapable of following some changes characteristic of autumn. Empirical values were consequently also approximated by splines, using the smooth splines procedure in R, and adjusting the degrees of freedom to make the fitted spline follow the main trend through the composite year without picking up too much variability within short time ranges.

Results

General seasonal models

In all our twelve species groups, the starting value of $\rho_{2.2}/\rho_{0.6}$ after the melting of snow in March and during the first week of April is found to remain between $2.2 \le a \le 2.4$ (Table 3). This is greater than the commonly assumed constant $\rho_{2.2}/\rho_{0.6}$ = 2. During the first ten days of April, the landscape-level $\rho_{2.2}/\rho_{0.6}$ value starts to increase (Figure 1), rapidly reaching an inflection point k_{pk} around day 140 (Table 3). The maximum values of $\rho_{2.2}/\rho_{0.6}$ occur in the vicinity of the summer solstice, around day 180. This is followed until the end of July by a slightly decreasing near-plateau. In August, an accelerated decrease of $\rho_{2.2}/\rho_{0.6}$ starts. This

process continues until the middle of September, by which the $\rho_{2.2}/\rho_{0.6}$ band ratio has decreased almost to 1.8. After this minimum is reached, an increase resumes, continuing until the end of October (the last month in our dataset). The season-ending value is about the same as the starting value.

However, the seasonal $\rho_{2.2}/\rho_{0.6}$ value for evergreen needleleaf forests is found not to depend so strongly on the time during the season. Although the 5-day averaged values indicate small fluctuations, variability around the mean values in each 5-day bin hides most of the possible seasonal changes, and the double logistic phenology model (1) predicts only a marginal increase for the mid-summer (Figure 2). This independence of the evergreen needleleaf $\rho_{2.2}/\rho_{0.6}$ value from the day of the year is indicated also by the almost zero value of the determination coefficient (Table 3).

Table 3. Estimated parameters for the model (1). An observation is one stand on an image granule. RSE is the model residual error. R^2 is the determination coefficient as defined by equation (2). Parameter values in the shaded cells were not significant. The parameter c has been fixed to the constant $c = 1$.

Tabel 3. Fenoloogiamudelile (1) lähendatud parameetrite väärtused. Parameeter c fikseeriti tasemele c = 1. Üks vaatlus moodustub ühe puistu spektraalsest heledusest ühe kuupäeva pildil. RSE on mudeli jääkviga, R^2 on arvutatud valemiga (2) ja halli taustaga lahtrites toodud hinnangud ei olnud statistiliselt olulised.

Model for group	N. obs			Parameter estimates / *Parameetrite hinnangud*						
Mudel grupile	*Arv*	R^2	RSE	a	b	d	k_{pk}	k_k	k_{ps}	k_s
All	5.6×10^6	0.15	0.69	2.22	2.22	1.24	140.0	5.84	262.4	22.0
Evergreen needleleaf	2.2×10^6	0.02	0.47	2.21	39.2	6.52	140.0	5.03	270.9	22.0
Deciduous broadleaf	1.4×10^6	0.45	0.68	2.34	1.22	0.95	138.0	4.50	255.0	25.0
Scots pine (MA)	1.0×10^6	0.05	0.43	2.20	160.0	5.61	136.9	*4.00*	262.3	21.0
MA (fertile soil)	6.3×10^5	0.05	0.43	2.21	160.0	5.41	141.0	*4.45*	264.7	23.0
MA (poor soil)	6.3×10^5	0.04	0.44	2.17	99.9	6.83	140.0	*4.61*	261.8	22.0
Norway spruce (KU)	6.3×10^5	0.02	0.56	2.19	5.55	6.13	150.0	8.00	280.0	22.0
Birch spp. (KS)	6.3×10^5	0.46	0.63	2.29	1.23	0.90	135.0	4.00	255.0	25.0
KS (fertile soil)	6.3×10^5	0.46	0.64	2.31	1.25	0.90	135.0	4.00	255.0	25.0
KS (poor soil)	6.3×10^4	0.45	0.66	2.24	1.19	0.90	137.4	4.00	255.0	25.0
European aspen (HB)	3.5×10^4	0.47	0.67	2.35	1.09	0.90	138.0	4.20	250.0	22.0
Grey alder (LV)	4.3×10^4	0.49	0.61	2.36	0.82	0.90	131.0	9.27	257.5	18.9

In contrast to the evergreen needleleaf tree species group, the deciduous broadleaved species group is found to exhibit substantial dependence on the date during the growth season (Figure 3). While there is not much difference in the springtime inflection point k_{pk}, the autumn inflection point k_{ps}, of the phenology model occurs 7 to 10 days earlier, in comparison both to the landscape average and to the evergreen needleleaf stands (Table 3). The autumn $\rho_{2.2}/\rho_{0.6}$ minimum is much more pronounced than in the landscape-level average (Figure 3). However, the model (1) is not flexible enough to capture such small fluctuations. On the other hand, the spline-based smoothed model (Table A2.1) follows the phenomena rather well. We find that during the autumn minimum the median values of $\rho_{2.2}/\rho_{0.6}$ can decrease even to about 1.5 for about 10 days.

Detailed models by tree species and soil fertility

The fitted parameters for particular tree species and soil fertility groups in model (1) follow the characteristics of the general groups that were defined in terms of pooled leaf type and pooled tree-shoot morphology. The run of seasonal $\rho_{2.2}/\rho_{0.6}$ values for Scots pine stands and Norway spruce stands is found to resemble the seasonal $\rho_{2.2}/\rho_{0.6}$ run for pooled evergreen forest (Figures A1.1 to A1.4). Similarly, the European aspen stands, birch stands, and grey alder stands are found to follow the seasonal $\rho_{2.2}/\rho_{0.6}$ run of the pooled deciduous broadleaved species group (Figures A1.5 to A1.9).

The tree species subsets do, however, exhibit some possible small, interesting time periods during which the empirical values of $\rho_{2.2}/\rho_{0.6}$ do not follow the phenology model (1).

(A) In the autumn, the three Scots pine stand groups and the Norway spruce stand group are found to exhibit a small decrease in $\rho_{2.2}/\rho_{0.6}$, similar to the $\rho_{2.2}/\rho_{0.6}$ decrease in the various deciduous broadleaved species groups. In the first Scots pine stand group (Scots pine overall, without differentiation by soil fertility) the decrease starts possibly already from day 230, with $\rho_{2.2}/\rho_{0.6}$ reaching its minimum value around day 270. In the Scots pine stands growing on poor soils this feature is more pronounced (Figure A1.3). In the Norway spruce stands group, the autumn minimum at the end of September is still more strongly pronounced (Figure A1.4). Each of the latter two groups includes a small proportion of deciduous broadleaved trees (Table 2), the share being about 10% in the case of the Norway spruce stands. This heterogeneity in stand composition partly explains the similarity with the broadleaved deciduous groups. Additionally, however, in the Estonian autumn about 25% of Scots pine needles turn yellow and are shed. This can cause seasonal reflectance changes similar to those exhibited by many broadleaved deciduous species.

(B) In the birch stand groups the seasonal changes in $\rho_{2.2}/\rho_{0.6}$ are found to follow those of the pooled deciduous broadleaved group. The autumn minimum is, however, more pronounced in the stands growing on fertile soils (as can be seen by comparing Figure A1.6 against Figures A1.5 and A1.7). The $\rho_{2.2}/\rho_{0.6}$

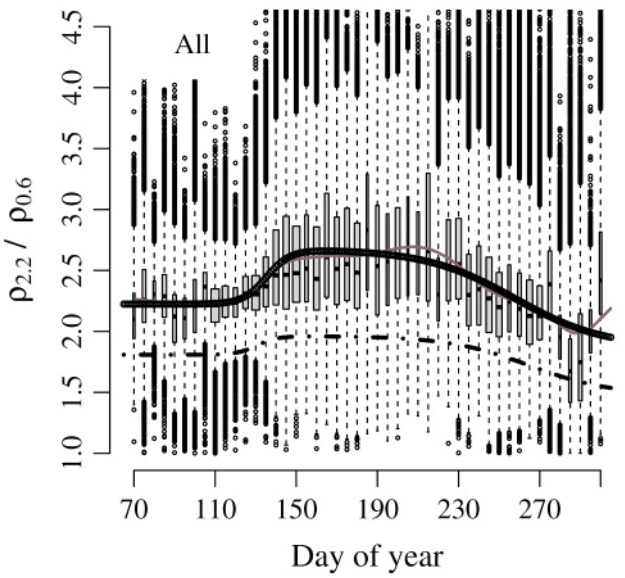

Figure 1. The average seasonal course of the red $\rho_{0.6}$ and near-infrared $\rho_{2.2}$ reflectance ratio, summarised as a boxplot using 5-day bins. The dashed line corresponds to the preliminary model estimated from USGS Landsat-8/9 OLI L2 surface reflectance data. The wide line corresponds to model (1); the narrower line to our spline-based refinement.

Joonis 1. Üldine keskmine 5-päevasteks intervallideks jaotatud punase $\rho_{0.6}$ ja lähi-infrapunase $\rho_{2.2}$ peegeldusteguri käik läbi kasvuperioodi. Jäme joon esitab mudeli (1), peenike joon näitab splainiga saadud lähendit ja katkendjoon näitab esialgset lähendit, mis saadi USGS Landsat-8/9 OLI atmosfäärikorrektsiooniga andmetest. X-teljel on päeva number aastas.

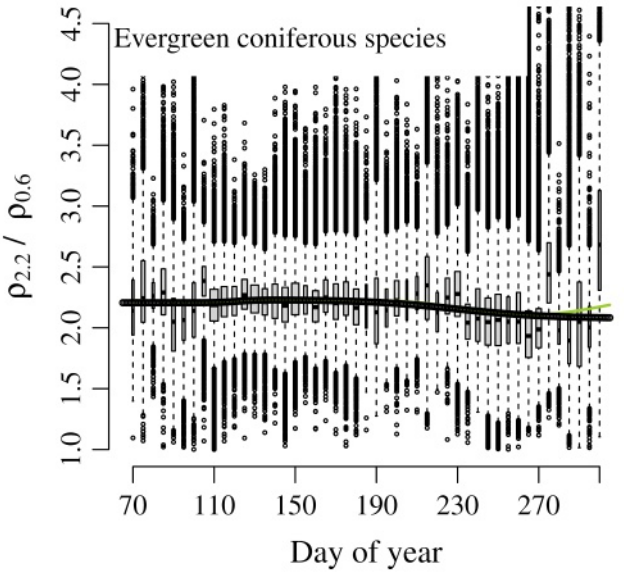

Figure 2. Evergreen needleleaf tree species group. Figure details are as in Figure 1.

Joonis 2. Igihaljad okaspuud. Täpsemad selgitused on joonise (1) allkirjas.

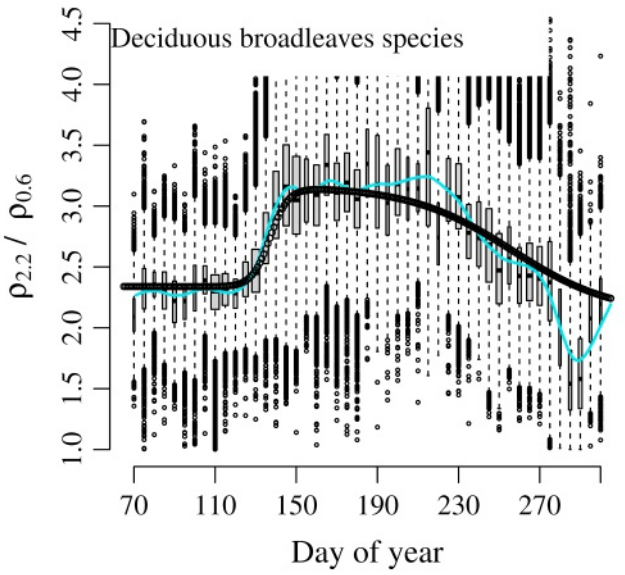

Figure 3. Deciduous broadleaved tree species group. Figure details are as in Figure 1.

Joonis 3. Heitlehiste lehtpuude grupp. Täpsemad selgitused on joonise (1) allkirjas.

value increases remarkably during the growth season, attaining values around 3 for several months. In the European aspen stands the $\rho_{2.2}/\rho_{0.6}$ value increases even more, with 5-day bin medians yielding $\rho_{2.2}/\rho_{0.6} \geq 3.25$ (Figure A1.8, Table A2.1). Otherwise, however, European aspen stands and birch stands exhibit similar seasonal values. The grey alder stands reach the greatest values of $\rho_{2.2}/\rho_{0.6}$ among all groups, with 5-day bin medians rising even as high as 3.5, and they differ somewhat in their seasonal courses from birch and European aspen stands (Figure A1.9, Table A2.1). There is in their case no rapid increase phase in the spring, with the $\rho_{2.2}/\rho_{0.6}$ seasonal course instead almost symmetrical around the summer solstice. Nevertheless, the springtime plateau before budburst is detectable, as in the other deciduous broadleaved species groups. An interesting pattern can be found during the late summer period, from day 250 until day 280, when the decrease in $\rho_{2.2}/\rho_{0.6}$ is replaced by a temporary increase before the final decrease sets in.

Discussion and Conclusion

Our study shows that the band ratio for dense dark vegetation represented by some common tree species found in the boreal and temperate climate regions is at almost all points in the snowless period greater than the commonly used value $\rho_{2.2}/\rho_{0.6} = 2$. Smaller values are found only during a short period in the autumn, when the yellowing of tree foliage marks the end of the growing season, and consequently substantially alters the canopy spectral reflectance signature. Evergreen needleleaf tree species have rather stable seasonal $\rho_{2.2}/\rho_{0.6}$ values. This stability contrasts with the substantial variation on the part of deciduous broadleaved tree species, for which the seasonal course of $\rho_{2.2}/\rho_{0.6}$ exhibits a variation dependent on the leaf area. During the most active growth period, the median values of $\rho_{2.2}/\rho_{0.6}$ increase up to 3.5 in deciduous broadleaved stands. Soil fertility has some, but rather small influence on the seasonal course of $\rho_{2.2}/\rho_{0.6}$.

Our findings agree well with published measurements of forested test sites where the regular normalised difference vegetation index (NDVI) reaches over 0.7, as NDVI does in our empirical dataset. For example, in the case of forests, Remer *et al.* (2001) report values of $\rho_{2.2}/\rho_{0.6}$ as high as about 4. The forest and dense-vegetation observations in the dataset of Kaufman *et al.* (1997) exhibit the range $1.7 \leq \rho_{2.2}/\rho_{0.6} \leq 3.4$, and de Almeida Castanho *et al.* (2007) find that $\rho_{2.2}/\rho_{0.6}$ for dark vegetation can increase even beyond 5. Admittedly, at the other end of the scale Karnieli *et al.* (2001), analysing aircraft measurements of various vegetated surfaces in Israel, find the $\rho_{2.2}/\rho_{0.6}$ close to 2. However, most of their samples have an NDVI of less than 0.7, which is less than the mean-value-subtracted-one standard deviation in our dataset (Table A3.1).

Despite this generally high value of $\rho_{2.2}/\rho_{0.6}$ in regions with NDVI > 0.7, evident both from our present study and from the above-cited literature, global environment optical data from Terra/Aqua MODIS and its successor constellation Suomi NPP VIIRS (Franch *et al.*, 2016) are routinely processed with the unrealistic $\rho_{2.2}/\rho_{0.6} = 2$ model – admittedly with some modifications that account for the scattering angle, and additionally account for foliage abundance on the basis of the vegetation index $NDVI_{SWIR}$ (Levy *et al.*, 2007). With these modifications, the model of Levy *et al.* (2007) yields a limited range of $1.5 < \rho_{2.2}/\rho_{0.6} < 2.1$ if calculated with the correct dependence on $NDVI_{SWIR}$ (Levy *et al.*, 2013) for the measurement geometry of Landsat-8/9 OLI and Sentinel-2 MSI, using vegetation index values that correspond to the forest canopies of our test area during the growth season. The discrepancy with the results of our present study stems from the spatial resolution of the data, i.e. from the pixel size. The MODIS-like environmental monitoring satellite scanners have a 250 to 500 m pixel size in the nadir view direction, in contrast with the 10 to 30 m pixels of Sentinel-2 MSI and Landsat-8/9 OLI. Such large pixels cover, as an example, more than ten forest stands, or several land cover classes, in the Estonian landscape. The inclusion of sparsely vegetated areas, bare soil, or buildings within the imaging depresses $\rho_{2.2}/\rho_{0.6}$ values, as shown in the case of urban areas by an empirical study of de Almeida Castanho *et al.* (2007), and by the model simulation experiments of Kaufman *et al.* (2002). Another influential factor is the prevalence of undetected small clouds, which likewise systematically depress $\rho_{2.2}/\rho_{0.6}$ values on such large pixels.

While the LaSRC algorithm used by USGS for the atmospheric correction of Landsat data already includes some accounting for seasonal and regional dependence of $\rho_{2.2}/\rho_{0.6}$, Sen2Cor still relies on the assumption of the constant $\rho_{2.2}/\rho_{0.6} = 2$. The inclusion of $\rho_{2.2}/\rho_{0.6}$ seasonal dependence into Sen2Cor would be technically simple. One option is to proceed as in LaSRC. Another option is to proceed from tree species maps. In the first implementations, these should distinguish

between evergreen forests and deciduous broadleaved forests, providing variables that support the prediction of seasonally correct $\rho_{2.2}/\rho_{0.6}$ values in 10–30 m pixels. Such maps, with suitable spatial resolution for Landsat-8/9 OLI and Sentinel-2 MSI data, do not at present exist globally, but nevertheless do exist at various national and regional levels, e.g. for Estonia (Lang *et al.*, 2018), Belgium (Bolyn *et al.*, 2022), Germany (Blickensdörfer *et al.*, 2024), Europe (Langanke *et al.*, 2018; Dostálová *et al.*, 2021), Argentina (Silveira *et al.*, 2023), and Canada (Hermosilla *et al.*, 2024).

Our present study leads us to conclude that so far as 10 to 30 m multispectral satellite imaging is concerned, the solution proposed by Kaufman *et al.* (1997) for atmospheric correction of at-sensor radiance is capable of substantial improvement. In our view, the integration of already collected satellite image time series with predictions of land surface reflectances yields the most promising approach to improving the accuracy of current atmospheric correction algorithms.

Acknowledgements. This study was supported by the Estonian Research Council grant PRG2214. Satellite images are distributed by USGS and ESA. We are grateful to Dr. Jérôme Louis from the Telespazio team for help with updating some features of Sen2Cor3. The authors thank Dr. Toomas Karmo for the linguistic and copy-edit review of the article manuscript. They also thank anonymous referees for reviewing their manuscript. Ground-surface elevation models and base-map data were provided by the Estonian Land Board.

References

Aasa, A., Jaagus, J., Ahas, R., Sepp, M. 2004. The influence of atmospheric circulation on plant phenological phases in central and eastern Europe. – International Journal of Climatology, 24(12), 1551–1564.

Arold, I. 2005. Estonian Landscapes. (Eesti maastikud). Tartu, Tartu Ülikooli Kirjastus. 253 pp. (In Estonian).

Baty, F., Ritz, C., Charles, S., Brutsche, M., Flandrois, J.-P., Delignette-Muller, M.-L. 2015. A toolbox for nonlinear regression in R: The package nlstools. – Journal of Statistical Software, 66(5), 1–21. https://doi.org/10.18637/jss.v066.i05.

Blickensdörfer, L., Oehmichen, K., Pflugmacher, D., Kleinschmit, B., Hostert, P. 2024. National tree species mapping using Sentinel-1/2 time series and German National Forest Inventory data. – Remote Sensing of Environment, 304, 114069. https://doi.org/10.1016/j.rse.2024.114069.

Bolyn, C., Lejeune, P., Michez, A., Latte, N. 2022. Mapping tree species proportions from satellite imagery using spectral–spatial deep learning. – Remote Sensing of Environment, 280, 113205. https://doi.org/10.1016/j.rse.2022.113205.

Chavez, P.S. Jr. 1988. An improved dark-object subtraction technique for atmospheric scattering correction of multispectral data. – Remote Sensing of Environment, 24(3), 459–479. https://doi.org/10.1016/0034-4257(88)90019-3.

de Almeida Castanho, A.D., Prinn, R., Martins, V., Herold, M., Ichoku, C., Molina, L.T. 2007. Analysis of visible/SWIR surface reflectance ratios for aerosol retrievals from satellite in Mexico City urban area. – Atmospheric Chemistry and Physics, 7(20), 5467–5477. hal-00296365. https://doi.org/10.5194/acp-7-5467-2007.

Domnich, M., Sünter, I., Trofimov, H., Wold, O., Harun, F., Kostiukhin, A., Järveoja, M., Veske, M., Tamm, T., Voormansik, K., Olesk, A., Boccia, V., Longepe, N., Cadau, E.G. 2021. KappaMask: AI-based cloudmask processor for Sentinel-2. – Remote Sensing, 13(20), 4100. https://doi.org/10.3390/rs13204100.

Dostálová, A., Lang, M., Ivanovs, J., Waser, L.T., Wagner, W. 2021. European wide forest classification based on Sentinel-1 data. – Remote Sensing, 13(3), 337. https://doi.org/10.3390/rs13030337.

Doxani, G., Vermote, E.F., Roger, J-C., Skakun, S., Gascon, F., Collison, A., De Keukelaere, L., Desjardins, C., Frantz, D., Hagolle, O., Kim, M., Louis, J., Pacifici, F., Pflug, B., Poilvé, H., Ramon, D., Richter, R., Yin, F. 2023. Atmospheric Correction Inter-comparison eXercise, ACIX-II Land: An assessment of atmospheric correction processors for Landsat 8 and Sentinel-2 over land. – Remote Sensing of Environment, 285, 113412. https://doi.org/10.1016/j.rse.2022.113412.

EE. 2025. Phenology calender in Estonia. (Eesti fenoloogiline kalender: Looduse fenoloogiline kalender Türil 1948.–95. aasta andmete põhjal (Eesti Meteoroloogia ja Hüdroloogia Instituudi andmebaas)). [WWW document]. – URL http://entsyklopeedia.ee/artikkel/eesti_fenoloogiline_kalender1. [Accessed 25 January 2025]. (In Estonian).

Eklundh, L., Jönsson, P. 2012. TIMESAT 3.1. Software Manual. Lund, Malmö, Sweden, Lund University and Malmö University. 82 pp.

ESA. 2021. S2 MPC Level-2A Algorithm Theoretical Basis Document. Ref. S2-PDGS-MPC-ATBD-L2A. Paris, France, European Space Agency (ESA). 78 pp. https://sentinels.copernicus.eu/documents/247904/446933/Sentinel-2-Level-2A-Algorithm-Theoretical-Basis-Document-ATBD.pdf/fe5bacb4-7d4c-9212-8606-6591384390c3?t=1643102691874.

Forest Act. 2023. Metsaseadus. – RT I, 22.09.2023, 3. (In Estonian).

Franch, B., Roger, J.C., Vermote, E.F. 2016. Suomi-NPP VIIRS surface reflectance Algorithm Theoretical Basis Document (ATBD). V1 Re-processing (NASA Land SIPS). Version 2.0. Greenbelt, Maryland, Goddard Space Flight Center. 33 pp.

Gatebe, C.K., King, M.D., Tsay, S.-C., Ji, Q., Arnold, G.T., Li, J.Y. 2001. Sensitivity of off-nadir zenith angles to correlation between visible and near-infrared reflectance for use in remote sensing of aerosol over land. – IEEE Transactions on Geoscience and Remote Sensing, 39(4), 805–819. https://doi.org/10.1109/36.917901.

Gustafsson, L., Baker, S.C., Bauhus, J., Beese, W.J., Brodie, A., Kouki, J., Lindenmayer, D.B., Lõhmus, A., Martínez Pastur, G., Messier, C., Neyland, M., Palik, B., Sverdrup-Thygeson, A., Volney, J., Wayne, A., Franklin, J.F. 2012. Retention forestry to maintain multifunctional forests: a world perspective. – BioScience, 62(7), 633–645. https://doi.org/10.1525/bio.2012.62.7.6.

Hermosilla, T., Wulder, M.A., White, J.C., Coops, N.C., Bater, C.W., Hobart, G.W. 2024. Characterizing long-term tree species dynamics in Canada's forested ecosystems using annual time series remote sensing data. – Forest Ecology and Management, 572, 122313. https://doi.org/10.1016/j.foreco.2024.122313.

Jaagus, J., Ahas, R. 2000. Space-time variations of climatic seasons and their correlation with the phenological development of nature in Estonia. – Climate Research, 15(3), 207–219. http://www.jstor.org/stable/24867314.

Karnieli, A., Kaufman, Y.J., Remer, L., Wald, A. 2001. AFRI — aerosol free vegetation index. – Remote Sensing of Environment, 77(1), 10–21. https://doi.org/10.1016/S0034-4257(01)00190-0.

Kaufman, Y.J., Gobron, N., Pinty, B., Widlowski, J-L., Verstraete, M.M. 2002. Relationship between surface reflectance in the visible and mid-IR used in MODIS aerosol algorithm - theory. – Geophysical Research Letters, 29(23), 2116. https://doi.org/10.1029/2001GL014492.

Kaufman, Y.J., Wald, A.E., Remer, L.A., Gao, B-C., Li, R-R., Flynn, L. 1997. The MODIS 2.1-μm channel — correlation with visible reflectance for use in remote sensing of aerosol. – IEEE Transactions on Geoscience and Remote Sensing, 35(5), 1286–1298.

Kõlli, R., Asi, E., Köster, T. 2004. Organic carbon pools in Estonian forest soils. – Baltic Forestry, 10(1), 19–26.

Kollist, P. 1967. On litterfall in transitional bog forests and the impact of drainage on it. (Puistu varisest siirdesoometsades ja kuivendamise mõjust sellele). – Metsanduslikud Uurimused, V, 148–163. (In Estonian with German and Russian summary).

Kuusk, J., Kuusk, A. 2018. Hyperspectral radiometer for automated measurement of global and diffuse sky irradiance. – Journal of Quantitative Spectroscopy and Radiative Transfer, 204, 272–280. https://doi.org/10.1016/j.jqsrt.2017.09.028.

Lang, M., Kaha, M., Laarmann, D., Sims, A. 2018. Construction of tree species composition map of Estonia using multispectral satellite images, soil map and a random forest algorithm. – Forestry Studies / Metsanduslikud Uurimused, 68, 5–24. https://doi.org/10.2478/fsmu-2018-0001.

Langanke, T., Herrmann, D., Ramminger, G., Buzzo, G., Berndt, F. 2018. Copernicus Land Monitoring Service – High resolution layer forest: Product specifications document. Version 11 of 2018-08-14. Copenhagen, Denmark, Copernicus Team at European Environment Agency (EEA). 38 pp.

Levy, R.C., Mattoo, S., Munchak, L.A., Remer, L.A., Sayer, A.M., Patadia, F., Hsu, N.C. 2013. The Collection 6 MODIS aerosol products over land and ocean. – Atmospheric Measurement Techniques, 6, 2989–3034. www.atmos-meas-tech.net/6/2989/2013/.

Levy, R.C., Remer, L.A., Mattoo, S., Vermote, E.F., Kaufman, Y.J. 2007. Second-generation operational algorithm: Retrieval of aerosol properties over land from inversion of Moderate Resolution Imaging Spectroradiometer spectral reflectance. – Journal of Geophysical Research: Atmospheres, 112, D13211. https://doi.org/10.1029/2006JD007811.

Liang, S., Fallah-Adl, H., Kalluri, S., Jájá, J., Kaufman, Y.J., Townshend, J.R.G. 1997. An operational atmospheric correction algorithm for Landsat Thematic Mapper imagery over land. – Journal of Geophysical Research: Atmospheres, 102(14), 17173–17186.

Nilson, T., Rautiainen, M., Pisek, J., Peterson, U. 2012. Seasonal reflectance courses of forests. – Oteng-Amoako, A.A. (ed.). New Advances and Contributions to Forestry Research. Rijeka, Croatia, IntechOpen, 33–58.

Nilson, T., Suviste, S., Lükk, T., Eenmäe, A. 2008. Seasonal reflectance course of some forest types in Estonia from a series of Landsat TM and SPOT images and via simulation. – International Journal of Remote Sensing, 29(17–18), 5073–5091. https://doi.org/10.1080/01431160802167543.

Ouaidrari, H., Vermote, E.F. 1999. Operational atmospheric correction of Landsat TM data. – Remote Sensing of Environment, 70(1), 4–15. https://doi.org/10.1016/S0034-4257(99)00054-1.

Pignatale, F.C., Louis, J., Müller-Wilm, U., Pflug, B. 2025. Sen2Cor 3.01.00 Software Configuration and User Manual, S2-SEN2LIKE-Sen2Cor_3.01.00-SUM_V1.1.pdf. [WWW document]. – URL https://github.com/senbox-org/sen2like/tree/master/sen2like/docs/source. [Accessed 20 January 2025].

Possen, B.J.H.M., Rousi, M., Silfver, T., Anttonen, M.J., Ruotsalainen, S., Oksanen, E., Vapaavuori, E. 2014. Within-stand variation in silver birch (*Betula pendula* Roth) phenology. – Trees, 28, 1801–1812. https://doi.org/10.1007/s00468-014-1087-x.

Raudsaar, M., Tamm, U., Pärt, E., Timmusk, T. 2023. Environment. – Sirkas, F., Valgepea, M. (eds.). Yearbook Forest 2021. Tallinn, Keskkonnaagentuur, 240–252.

Rautiainen, M., Lukeš, P., Homolová, L., Hovi, A., Pisek, J., Mõttus, M. 2018. Spectral properties of coniferous forests: A review of *in situ* and laboratory measurements. – Remote Sensing, 10(2), 207. https://doi.org/10.3390/rs10020207.

R Core Team. 2022. R: A language and environment for statistical computing. R Foundation for Statistical Computing, Vienna, Austria. [WWW document]. – URL https://www.R-project.org/. [Accessed 6 October 2022].

Remer, L.A., Levy, R.C., Mattoo, S., Tanré, D., Gupta, P., Shi, Y., Sawyer, V., Munchak, L.A., Zhou, Y., Kim, M., Ichoku, C., Patadia, F., Li, R-R., Gassó, S., Kleidman, R.G., Holben, B.N. 2020. The dark target algorithm for observing the global aerosol system: past, present, and future. – Remote Sensing, 12(18), 2900. https://doi.org/10.3390/rs12182900.

Remer, L.A., Wald, A.E., Kaufman, Y.J. 2001. Angular and seasonal variation of spectral surface reflectance ratios: Implications for the remote sensing of aerosol over land. – IEEE Transactions on Geoscience and Remote Sensing, 39(2), 275–283.

Saunier, S., Pflug, B., Lobos, I.M., Franch, B., Louis, J., De Los Reyes, R., Debaecker, V., Cadau, E.G., Boccia, V., Gascon, F., Kocaman, S. 2022. Sen2Like: Paving the way towards harmonization and fusion of optical data. – Remote Sensing, 2022, 14(16), 3855. https://doi.org/10.3390/rs14163855.

Sayler, K., Glynn, T. 2022. Landsat 9 Data Users Handbook. LSDS-2082, Version 1.0. Sioux Falls, South Dakota, Department of the Interior, U.S. Geological Survey (USGS). 107 pp.

Sellin, A., Heinsoo, K., Kupper, P., Meier, R., Õunapuu-Pikas, E., Reinthal, T., Rosenvald, K., Tullus, A. 2024. Growth responses to elevated environmental humidity vary between phenological forms of *Picea abies*. – Frontiers in Forests and Global Change, 7, 1370934. https://doi.org/10.3389/ffgc.2024.1370934.

Silveira, E.M.O., Radeloff, V.C., Martinuzzi, S., Martinez Pastur, G.J., Bono, J., Politi, N., Lizarraga, L., Rivera, L.O., Ciuffoli, L., Rosas, Y.M., Olah, A.M., Gavier-Pizarro, G.I., Pidgeon, A.M. 2023. Nationwide native forest structure maps for Argentina based on forest inventory data, SAR Sentinel-1 and vegetation metrics from Sentinel-2 imagery. – Remote Sensing of Environment, 285, 113391. https://doi.org/10.1016/j.rse.2022.113391.

Suviste, S., Nilson, T., Lükk, T., Eenmäe, A. 2007. Seasonal reflectance course of some forest types in Estonia from multi-year Landsat TM and SPOT images and via simulation. – Proceedings of the International Workshop on the Analysis of Multi-temporal Remote Sensing Images, Belgium, July 2007. Leuven, 1–5. https://doi.org/10.1109/MULTITEMP.2007.4293068.

Tamm, Ü. 2000. Aspen in Estonia. (Haab Eestis). – Tartu, Eesti Loodusfoto. 257 pp. (In Estonian).

Tappo, E. 1982. Mean characteristics of forest stands in Estonia by dominant species, site fertility, and age. (Eesti NSV puistute keskmised takseertunnused puistu enamuspuuliigi, boniteedi ja vanuse järgi). Tallinn, Eesti NSV Põllumajandusministeeriumi Informatsiooni ja Juurutamise Valitsus. 72 pp. (In Estonian.)

Turner, R.E., Spencer, M.M. 1972. Atmospheric model for correction of spacecraft data. – Proceedings of the 8th International Symposium on Remote Sensing of Environment, United States, October 1972. Ann Arbor, Michigan, 895–934.

Valgepea, M., Sirkas, F., Timmusk, T., Pärt, E., Suursild, E., Matson, T. 2023. Forest resources. – Sirkas, F., Valgepea, M. (eds.). Yearbook Forest 2021. Tallinn, Keskkonnaagentuur, 17–96.

Vermote, E., Justice, C., Claverie, M., Franch, B. 2016. Preliminary analysis of the performance of the Landsat 8/OLI land surface reflectance product. – Remote Sensing of Environment, 185, 46–56. https://doi.org/10.1016/j.rse.2016.04.008.

Zanter, K. 2016. Landsat 8 (L8) Data Users Handbook. LSDS-1574, Version 2.0. Sioux Falls, South Dakota, Department of the Interior, U.S. Geological Survey (USGS). 98 pp.

Submitted February 6, 2025, accepted August 12, 2025

The journal is financially supported by the Estonian Environmental Investment Centre and the Institute of Forestry and Engineering of the Estonian University of Life Sciences

Sateliidipiltide atmosfäärikorrektsiooniks kasutatava tiheda taimkatte 660 nm ja 2200 nm spektraalkanalites mõõdetud peegeldustegurite suhte sõltuvus puistu enamuspuuliigist ja kasvuperioodist

Mait Lang, Lea Hallik ja Allan Sims

Kokkuvõte

Spektri optilises piirkonnas (300–2500 nm) satelliitidelt Maa pinna kirkuse mõõtmisi mõjutab atmosfääri gaasides kiirguse neeldumine, Rayleigh' hajumine ning aerosooliosakestelt hajumine ja neeldumine (Turner & Spencer, 1972). Atmosfäärist tuleneva mõju kõrvaldamiseks kasutatakse laialdaselt tumeda maapealse objekti meetodit (Chavez, 1988), sest nii mõõdetav signaal pärineb eeldatavalt põhiliselt atmosfäärist. Kaufman *et al.* (1997) leidsid, et tihe taimkate sobib maapealseks tumedaks objektiks, ja pakkusid, et spektri punase (0.6 µm) piirkonna peegeldusteguri saab prognoosida lühilainelise infrapunase spektriosa (2.2 µm) järgi kasutades suhet $\rho_{2.2}/\rho_{0.6}$ = 2, mille kehtivust kinnitati üldjoontes empiiriliste (Remer *et al.*, 2001) ja teoreetiliste (Kaufman *et al.*, 2002) uuringutega. See suhe on teatud väikeste muudatustega kasutusel operatiivsetes atmosfääri-korrektsiooni algoritmides tänaseni (Liang *et al.*, 1997; Ouaidrari & Vermote 1999; Levy *et al.*, 2007, 2013; Vermote *et al.*, 2016). Siiski näitasid nii eeltoodud tööd ja on teada ka Eestis tehtud empiirilistest uuringutest (Suviste *et al.*, 2007; Nilson *et al.*, 2008, 2012), et taimestikus esineb loomulik peegeldusteguri variatsioon, mis sõltub fenofaasist ja $\rho_{2.2}/\rho_{0.6}$ võib oluliselt erineda konstandist 2. Kuna Landsat-8/9 OLI ja Sentinel-2 MSI ülesvõtete aegread on oluliseks sisendiks metsade seirel, siis on vaja vältida piltide atmosfäärikorrektsioonist tulenevaid vigu. Siinse uurimuse eesmärk oli analüüsida suhte $\rho_{2.2}/\rho_{0.6}$ sõltuvust metsa fenofaasist, sest see suhe on kasutusel laialt levinud atmosfäärikorrektsioonipaketis Sen2Cor, mille haruversiooniga töödeldakse nii Landsat-8/9 OLI kui ka Sentinel-2 MSI andmeid (Saunier *et al.*, 2022; Pignatale, *et al.*, 2025). Metsaregistrist valiti riigimetsade puistud, mis olid vanemad kui 15 aastat ja jagati need enamuspuuliigi ja boniteedi järgi rühmadesse (tabelid 1, 2, A3.1). Analüüsiks laaditi alla Maa-ameti serverist Sentinel-2 MSI atmosfäärivälise kirkuse (L1C) andmed ja USGS andmebaasist Landsat-8/9 OLI atmosfäärivälise kirkuse (L1) ja maapinna peegeldusteguri (L2) andmed. Selgus, et L2 andmetes on tootmisviga, aga piltide tasemel keskväärtused sobisid kanalite suhte fenoloogiamudeli (1) esialgsete parameetrite leidmiseks. Mudelit (1) sobitati seejärel Sen2Cor3 abil arvutatud spektraalse peegeldusteguri aegrea andmetele. Saadud mudeliga prognoositi aegrea piltidele $\rho_{2.2}/\rho_{0.6}$ ülesvõtte kuupäevast sõltuvad väärtused ja saadi seejärel täpsustatud atmosfäärikorrektsiooniga piltidelt kõikidele puistutele spektraalsed peegeldustegurid. Puistute andmestikus lähendati puuliigi-rühmades mudeli (1) parameetrid (tabel 2) ja empiirilised andmed lähendati ka splaini abil (tabel A2.1.). Maastiku tasemel puistute keskmisena ilmnes suhte $\rho_{2.2}/\rho_{0.6}$ selge sõltuvus fenofaasist (joonis 1), mis samas praktiliselt puudus igihaljastes okasmetsades (joonised 2, A1.1, A1.2, A1.3, A1.4), aga oli seda suurem heitlehistes lehtpuumetsades (joonised 3, A1.5, A1.6, A1.7, A1.8, A1.9). Olulist sõltuvust mullaviljakusest ei täheldatud, aga sügisene lehtede kolletumine ilmnes empiirilistes andmetes, kuigi oli lähendatav ainult splaini abil, sest mudeli (1) kuju ei võimalda selliseid lühiajalisi võnkumisi kirjeldada. Uurimuse tulemusena koostatud mudelid saab lihtsasti lõimida Sen2Cor algoritmi ja piirkonniti on juba olemas suhte $\rho_{2.2}/\rho_{0.6}$ fenofaasile vastava väärtuse prognoosmudeli rakendamiseks vajalikud puistute liigilise koosseisu kaardid (Lang *et al.*, 2018; Bolyn *et al.*, 2022; Blickensdörfer *et al.*, 2024; Langanke *et al.*, 2018; Dostálová *et al.*, 2021; Silveira *et al.*, 2023; Hermosilla *et al.*, 2024).

Appendix 1. Detailed models for tree species and soil fertility groups.

Lisa 1. Mudelid puuliikide ja mullaviljakuse klasside kaupa.

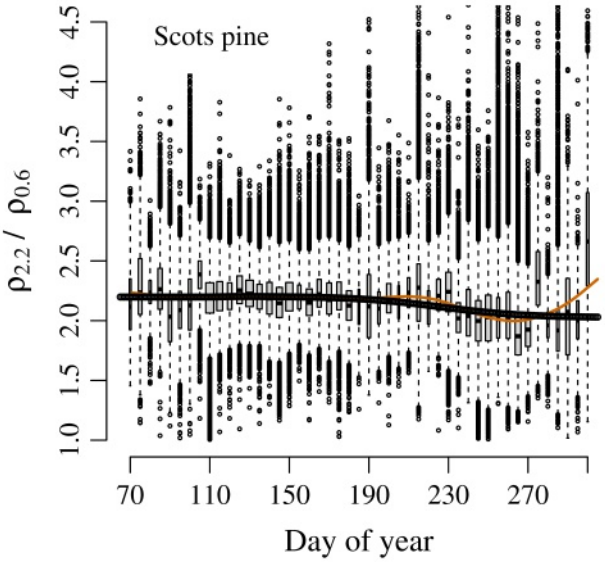

Figure A1.1. Scots pine stands.

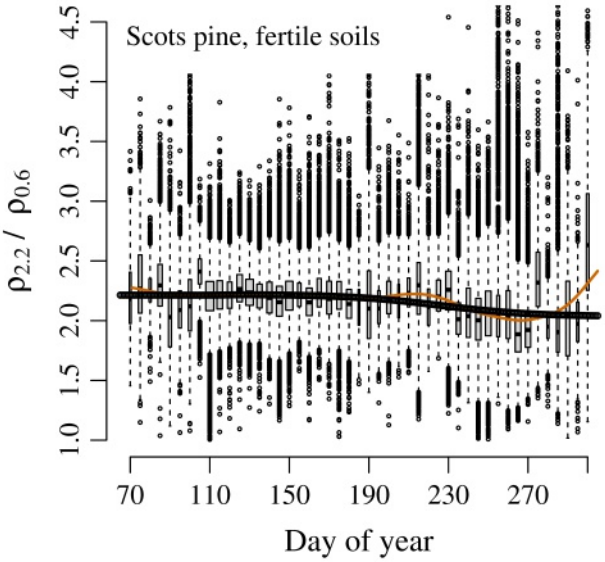

Figure A1.2. Scots pine stands on fertile soils.

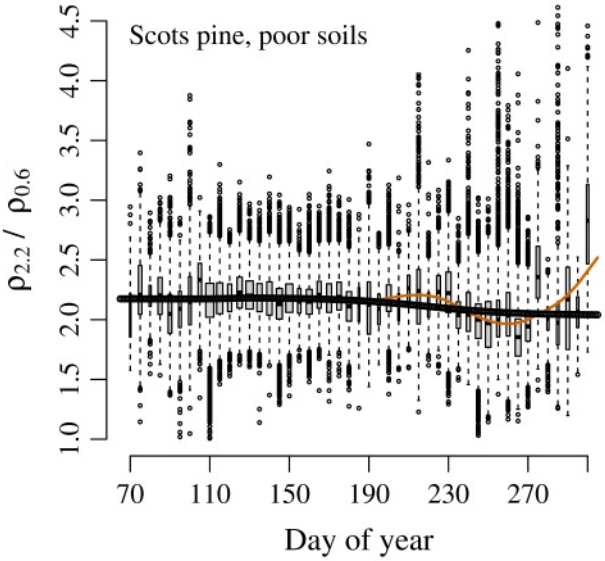

Figure A1.3. Scots pine stands on poor soils.

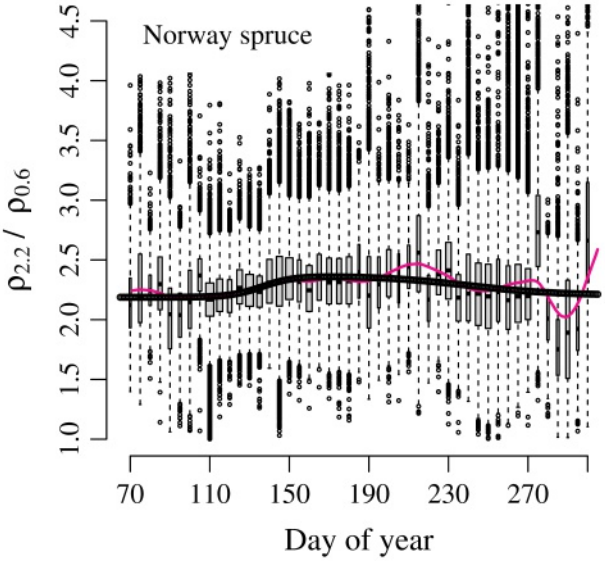

Figure A1.4. Norway spruce stands.

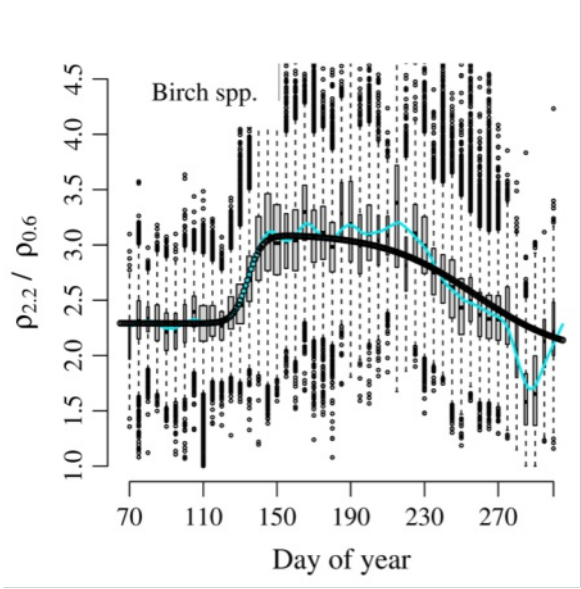

Figure A1.5. Birch stands.

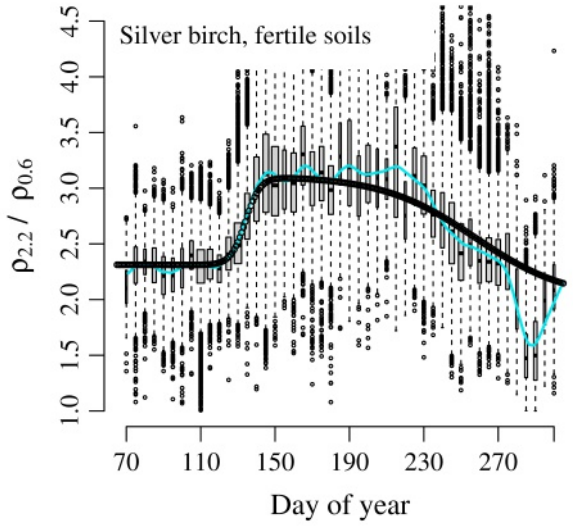

Figure A1.6. Birch stands on fertile soils.

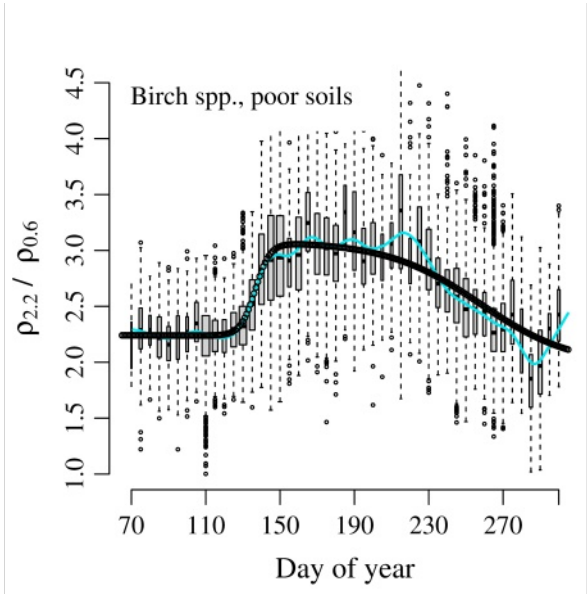

Figure A1.7. Birch stands on poor soils.

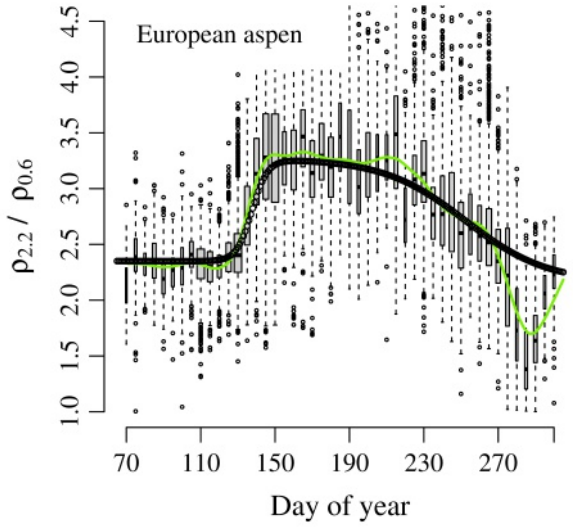

Figure A1.8. European aspen stands.

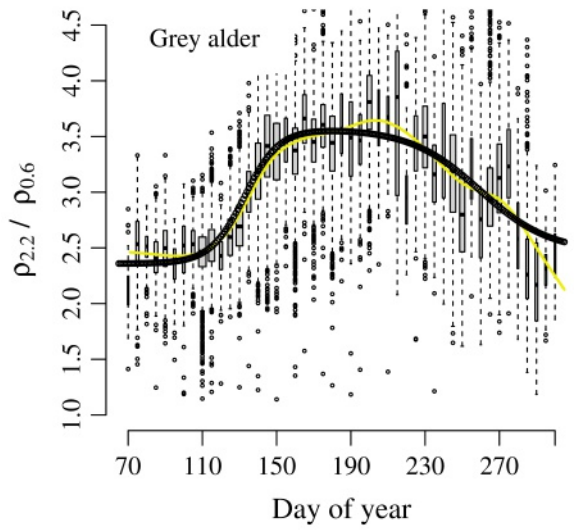

Figure A1.9. Grey alder stands.

Appendix 2. Smoothed course of the near-infrared/red reflectance ratio $\rho_{2.2}/\rho_{0.6}$.

Lisa 2. Punase $\rho_{0.6}$ ja lähi-infrapunase spektriosa $\rho_{2.2}$ peegeldustegurite suhte $\rho_{2.2}/\rho_{0.6}$ silutud aegrida.

Table A2.1. Smoothed course of the near-infrared/red reflectance ratio $\rho_{2.2}/\rho_{0.6}$. Values are scaled by 100. Group descriptions are given in Tables 1 and 2.

Tabel A2.1. Punase $\rho_{0.6}$ ja lähi-infrapunase spektriosa $\rho_{2.2}$ peegeldustegurite suhte $\rho_{2.2}/\rho_{0.6}$ silutud aegrida. Väärtused on skaleeritud kordajaga 100. Gruppide kirjeldused on tabelites (1) ja (2).

Day / *Päev*	Tree species groups / *Puuliikide rühmad*											
	All	Everg. N.	Dec. Br.	MA-A	MA-F	MA-P	KU-A	KS-A	KS-F	KS-P	HB-A	LV-A
70	226	223	226	224	228	220	224	225	222	229	233	246
73	226	223	228	223	227	220	225	229	227	229	233	246
76	226	222	230	222	226	219	225	231	231	228	233	245
79	225	222	231	222	225	218	225	232	232	226	232	245
82	224	222	230	221	224	218	224	231	232	224	231	245
85	223	222	229	221	223	217	222	229	229	223	231	244
88	222	222	227	220	222	216	220	226	226	221	230	244
91	222	222	226	220	222	216	219	224	224	221	230	243
94	221	222	227	220	221	216	218	224	224	223	230	243
97	221	222	228	220	221	216	219	226	226	224	231	243
100	221	222	230	220	221	217	220	229	229	226	232	243
103	222	222	232	220	221	217	220	232	232	227	233	244
106	222	222	232	220	221	217	220	233	233	227	233	245
109	222	222	231	220	221	217	219	231	231	226	232	246
112	223	222	230	220	222	218	219	230	230	224	231	248
115	223	222	229	221	222	218	219	229	229	222	229	251
118	225	222	229	221	222	219	220	228	229	222	228	254
121	227	222	231	221	223	219	222	230	231	222	229	259
124	229	222	234	221	223	219	224	234	236	224	233	265
127	232	222	240	221	223	220	225	239	242	228	239	272
130	236	222	250	221	223	219	226	248	252	235	250	280
133	241	222	265	221	222	219	227	262	267	246	266	289
136	245	222	281	221	222	219	229	278	283	261	285	298
139	250	223	296	220	221	218	231	293	297	275	302	308
142	253	223	307	220	220	217	232	304	307	287	316	316
145	256	223	314	219	220	217	233	311	313	293	326	324
148	258	223	316	219	220	217	234	312	314	296	330	330
151	260	223	314	219	220	217	234	308	310	296	330	336
154	260	223	312	219	220	217	233	304	307	295	329	340
157	261	223	312	219	220	217	232	304	306	297	330	343
160	261	223	314	219	220	217	232	309	310	302	331	345
163	262	223	318	219	220	217	233	315	316	308	332	347
166	262	223	321	219	220	217	234	319	320	312	333	349
169	262	223	320	219	220	217	234	317	318	311	332	350
172	262	223	318	218	219	217	234	312	312	308	330	351
175	262	223	315	218	219	216	234	307	308	304	328	352
178	262	223	313	218	219	216	233	304	305	303	327	353
181	262	223	313	218	218	215	233	306	307	304	326	354
184	263	223	315	218	218	215	232	312	313	307	326	356
187	264	223	317	218	218	215	232	317	318	310	326	357
190	264	223	318	219	219	216	232	318	320	310	325	359
193	266	222	318	219	219	216	234	315	318	307	324	361
196	267	222	318	219	220	217	236	311	314	304	323	363
199	268	222	319	220	220	218	238	310	312	302	323	364
202	269	222	320	220	221	219	241	311	313	302	324	365
205	269	222	322	220	222	219	243	312	314	304	326	364
208	269	221	323	220	222	220	245	314	315	307	328	363

Table A2.1. Continues.

Tabel A2.1. Jätkub.

Day / *Päev*	Tree species groups / *Puuliikide rühmad*											
	All	Everg. N.	Dec. Br.	MA-A	MA-F	MA-P	KU-A	KS-A	KS-F	KS-P	HB-A	LV-A
211	269	221	324	220	222	220	247	317	317	311	328	362
214	268	220	325	220	222	221	247	320	319	315	328	360
217	267	220	323	219	222	221	246	320	319	316	325	357
220	265	219	320	219	221	220	244	316	315	313	321	353
223	262	218	315	218	220	219	242	311	311	309	317	349
226	259	218	311	216	219	218	240	305	306	302	312	345
229	255	217	306	215	217	216	237	300	302	294	307	341
232	251	216	299	213	215	214	234	293	296	285	301	336
235	247	215	291	211	213	211	231	283	286	276	294	331
238	242	214	282	209	211	208	228	274	276	269	287	326
241	239	214	275	208	209	206	226	266	267	263	282	321
244	235	213	269	206	207	203	224	261	261	258	278	316
247	232	212	264	204	206	201	224	257	256	255	275	312
250	230	212	259	203	205	199	224	252	251	252	273	308
253	228	211	256	202	204	198	225	249	249	249	271	305
256	226	211	254	201	203	197	227	247	247	246	270	303
259	224	211	253	200	202	197	229	244	245	243	268	301
262	223	211	252	200	201	197	230	242	242	239	265	300
265	221	211	250	200	200	197	231	239	239	236	258	298
268	219	211	246	200	200	199	232	236	237	233	248	296
271	216	211	240	201	201	201	233	234	233	231	235	292
274	213	211	230	203	202	203	232	228	227	227	220	288
277	209	212	217	204	203	206	228	216	213	221	204	282
280	205	212	201	206	205	209	219	199	193	212	189	276
283	202	213	186	208	206	212	210	182	174	204	177	268
286	199	213	176	211	209	215	204	171	161	199	171	260
289	198	214	173	214	212	219	202	170	159	200	170	253
292	200	215	177	217	216	224	206	179	166	206	175	245
295	202	216	184	221	221	230	213	192	178	215	183	237
298	207	217	194	225	227	236	225	204	190	224	193	230
301	212	218	205	229	233	243	239	215	202	233	204	222
304	217	218	216	233	239	250	254	225	212	241	215	215
307	223	219	227	238	246	257	269	235	223	249	226	208
310	228	220	238	242	252	263	284	245	234	257	237	200

Appendix 3. The normalised difference vegetation index (NDVI) in tree species groups.

Lisa 3. Normeeritud vahe indeks (NDVI) puuliigigruppide kaupa.

Table A3.1. The normalised difference vegetation index $I_{NDVI} = (\rho_{0.85} - \rho_{0.6}) / (\rho_{0.85} + \rho_{0.6})$ mean values and standard deviation for our species groups. Spectral reflectances are from the bands at 0.85 µm ($\rho_{0.85}$) and 0.6 µm ($\rho_{0.6}$). Group descriptions are given in Tables 1 and 2. The estimate is made for the period starting from day 141 and ending with day 259.

Tabel A3.1. Normeeritud vahe indeksi $I_{NDVI} = (\rho_{0.85} - \rho_{0.6}) / (\rho_{0.85} + \rho_{0.6})$ keskväärtus ja standardhälve puuliigigruppide kaupa. Spektraalsed peegeldustegurid on võetud lainepikkustele 0.85 µm ($\rho_{0.85}$) ja 0.6 µm ($\rho_{0.6}$) vastavatest kanalitest. Hinnang kehtib päevade vahemikule 141–259. Gruppide kirjeldused on tabelites (1) ja (2).

Tree species group / *Puuliikide rühm*		NDVI	
Species / *Puuliigid*	Bonity / *Boniteedid*	Mean / *Keskmine*	Standard deviation / *Standardhälve*
All	A	0.79	0.09
Everg. N.	A	0.78	0.06
Dec. Br.	A	0.78	0.13
MA	A	0.77	0.06
MA	F	0.78	0.06
MA	P	0.76	0.06
KU	A	0.82	0.07
KS	A	0.77	0.13
KS	F	0.78	0.13
KS	P	0.75	0.15
HB	A	0.78	0.15
LV	A	0.79	0.14